SOFT ROBOTS

Millimeter-scale flexible robots with programmable three-dimensional magnetization and motions

Tianqi Xu, Jiachen Zhang, Mohammad Salehizadeh, Onaizah Onaizah, Eric Diller*

Flexible magnetic small-scale robots use patterned magnetization to achieve fast transformation into complex three-dimensional (3D) shapes and thereby achieve locomotion capabilities and functions. These capabilities address current challenges for microrobots in drug delivery, object manipulation, and minimally invasive procedures. However, possible microrobot designs are limited by the existing methods for patterning magnetic particles in flexible materials. Here, we report a method for patterning hard magnetic microparticles in an elastomer matrix. This method, based on ultraviolet (UV) lithography, uses controlled reorientation of magnetic particles and selective exposure to UV light to encode magnetic particles in planar materials with arbitrary 3D orientation with a geometrical feature size as small as 100 micrometers. Multiple planar microrobots with various sizes, different geometries, and arbitrary magnetization profiles can be fabricated from a single precursor in one process. Moreover, a 3D magnetization profile allows higher-order and multi-axis bending, large-angle bending, and combined bending and torsion in one sheet of polymer, creating previously unachievable shape changes and microrobotic locomotion mechanisms such as multi-arm power grasping and multi-legged paddle crawling. A physics-based model is also presented as a design tool to predict the shape changes under magnetic actuation.

INTRODUCTION

Millimeter- and micrometer-scale robots have a growing number of potential applications in healthcare, bioengineering, and microfactories (*1*–*4*). Because such microrobots are subject to microscale physics and dynamics, the actuation mechanisms commonly used differ from those for traditional large-scale robots. Common microrobot actuation mechanisms use piezoelectric actuators (*5*, *6*), stimuli-responsive materials (*7*–*9*), chemical fuel (*10*), acoustic radiation force driving (*11*, *12*), and optothermal trapping (*13*, *14*). These mechanisms have been used to design various types of artificial muscles and self-folding structures, demonstrating their utility for high-precision applications despite the compact designs. However, there are trade-offs among response speed, ease of access and control, and available shapes of transformation. Thus, untethered microrobots that have programmable three-dimensional (3D) deformation and instantaneous response are still not fully achieved.

Magnetic actuators are distinguished for their fast response to input signals and the ability to be controlled wirelessly in confined spaces. In addition, safe robot-human interaction and lower cost make them ideal tools for in vivo disease diagnosis and treatment (*15*–*17*). To date, most studies have focused on rigid magnetic microrobots. Although these robots have no more than five actuated degrees of freedom under a magnetic field, their geometries are designed to convert simple translation and rotation into functional motions for applications such as targeted drug delivery (*17*–*20*), cell culture (*21*), assisted fertilization (*22*), and noninvasive medical intervention inside the vascular system (*23*). However, because these microrobots are confined by the simple uniform distribution of magnetic moments in a rigid body, they lack the ability to form internal deformation, which is necessary for sophisticated motions such as grasping and crawling. To overcome these limitations, flexible magnetic materials that have programmable morphologies can be used (*24*).

Department of Mechanical and Industrial Engineering, Microrobotics Laboratory, University of Toronto, 5 King's College Rd., Toronto, Ontario M5S 3G8, Canada.
*Corresponding author. Email: ediller@mie.utoronto.ca

Programmable morphologies of flexible magnetic materials are realized by patterning magnetic particles in a polymer composite. The magnetic particles can either be magnetically soft, not retaining their magnetization when an applied magnetic field is removed, or magnetically hard, retaining some magnetization. Soft magnetic particles can be synthesized at the nanometer size (*25*) and can be lithographically patterned into hydrogel sheets (*26*, *27*) or other artificial composites (*28*). The morphology of the hydrogel sheets is programmed by the formation of aligned soft magnetic nanoparticle chains, which function as preferred magnetic axes, and components to reinforce material rigidity. In comparison, hard magnetic particles can be synthesized only at micrometer or larger size, but the remanent magnetization of premagnetized particles enables more sophisticated capabilities, such as complex locomotion modes (*29*–*31*), object manipulation and assembly (*32*–*34*), and fast 3D transformation (*35*). Different techniques for patterning hard magnetic particles have been used to realize the heterogeneous magnetization and thus the independent addressability to different parts with a global actuating magnetic field (Table 1).

However, previous patterning methods still cannot achieve all types of magnetic torque-induced deformations because the ability to precisely pattern discrete 3D magnetization in planar soft materials has not been shown. Such capability would enable new types of sophisticated microrobotic devices with programmable shape changes. For example, we show multi-arm structures that can transform into a hollow sphere under a static magnetic field. To date, microrobots that have discrete 3D magnetization profiles and patterned shapes below centimeter size can be fabricated only by manual microassembly of magnetic components, but the cost and difficulty rise markedly in association with decreased size, increased number of parts, and magnetization complexity.

Here, we report an ultraviolet (UV) lithography–based method to encode 3D magnetization in planar flexible composites at the submillimeter scale. Similar to photolithography-based patterning technique for soft magnetic particles (*26*–*28*), in this method, we precisely reoriented premagnetized permanent magnetic particles and then selectively cured UV resin to pattern the local magnetization.

Table 1. Capabilities of major existing methods to pattern magnetic particles. 1D: Only binary magnetization can be patterned, e.g., longitudinal or perpendicular recording in a hard disk drive. 2D: Direction of magnetization in each layer is restricted to a single plane. 3D: Magnetization in each layer can be patterned in arbitrary direction. Discrete: Magnetization in each area is independent of adjacent areas. Continuum: Magnetization in each area cannot have sudden changes with respect to adjacent areas. N/A, not applicable.

Method	Magnet type	Shape of media*	Template or mold required	States of magnetization†
Electrodeposition of magnetic particles on lithographically printed microstructures (*18*, *21*, *22*)	Soft	3D	No	N/A
Lithographic patterning of magnetic nanoparticles (*26*–*28*)	Soft	2D	No	Discrete, 3D
Magnetic particles linked by DNA (*44*)	Soft	N/A	No	Discrete, 1D
Microassembly of magnetic components (*33*, *34*, *45*)	Hard	3D	Yes	Discrete, 3D
Magnetic recording technology (*46*)	Hard	2D	No	Discrete, 1D
Template-aided magnetizing (*29*–*31*)	Hard	2D	Yes	Continuum, 3D
3D printing of ferromagnetic domains (*35*)	Hard	3D	No	Discrete, 2D
This work	Hard	2D	No	Discrete, 3D

*Shape of media refers to the structure of the composite materials in which the magnetic particles are dispersed. 2D refers to planar structures, whereas 3D refers to solid 3D structures. †States of magnetization is defined as degrees of freedom related to the orientation of hard magnetic particles or preferred magnetic axes of soft magnetic particles in each area.

Multiple microrobots that have different geometries and 3D magnetization profiles could be fabricated from the same precursor in a single process. We achieved a geometrical feature size as small as 100 μm by 100 μm and precise magnetization feature size as small as 250 μm by 250 μm on an 80-μm-thick UV resin layer. Using this method, we fabricated millimeter-scale structures that exhibited higher-order and multi-axis deformation, large-angle bending, or combined bending and torsion. We also present new microrobotic capabilities enabled by this technique and provide a model to predict the shape changes that can be used as a design tool.

RESULTS

Patterning discrete 3D magnetization

In this work, discrete means that local magnetization can have sudden changes with respect to adjacent areas. 3D refers to the degrees of freedom related to the orientation of integrated magnetic particles. The ability to precisely program discrete 3D magnetization in flexible materials can enable planar actuators that have arbitrary distribution of magnetic torque. The desired magnetic torque distribution, expressed as a function of location, can be directly mapped to the magnetization profile of the sheet if the size of each magnetization area is sufficiently small. In addition to precise patterning, discrete 3D magnetization can enhance the performance of magnetic actuators and introduce new designs. For simple bending or torsion, local magnetization can be programmed to maintain 90° with respect to the actuating field to maximize deformation, making it possible for millimeter-scale actuators to have large deformations under a weaker actuating magnetic field. New shape changes are enabled by the capability to pattern highly discontinuous magnetization profiles in complex geometries. For example, we show planar structures that have multiple unparalleled bending axes and large bending angles (as large as 180°) under a static magnetic field.

Figure 1A shows the physical apparatus for patterning 3D discrete magnetization in planar UV-curable materials. The materials in the substrate were prepared by mixing premagnetized hard magnetic particles with flexible UV resin. With the three-axis Hall effect sensor providing feedback data, the cube permanent magnet under the substrate could generate a magnetic field to precisely reorient all the magnetic particles included in the UV resin. After particle reorientation, the digital light processing (DLP) projector emitted UV light on selected regions of the substrate, which initiated polymerization and froze the magnetic particles within those regions. This automated two-step patterning procedure can be optionally repeated depending on the complexity of the actuator design. Movie S1 shows the automated fabrication process. Figure 1B shows the influence of magnetic particle concentration on UV penetration depth. As the mass ratio approached 1.5:1, the magnetic slurry became highly viscous and the difficulty of reorienting the particles increased markedly. Therefore, we recommend that the mass ratio of magnetic particles and UV resin be controlled at 1:1 or lower for better patterning precision. Here, we used 1:1 as the default mass ratio, unless mentioned otherwise.

In this work, we mainly demonstrate the capability to pattern discrete 3D magnetization in planar materials, but this technique has potential to be extended to 3D structures due to the well-established DLP-based 3D printing technique. As a primary demonstration, Fig. 1 (C and D) shows a dual-layer structure patterned using a manual material feeding approach. The fabrication procedure for the dual-layer structure is described in text S1.

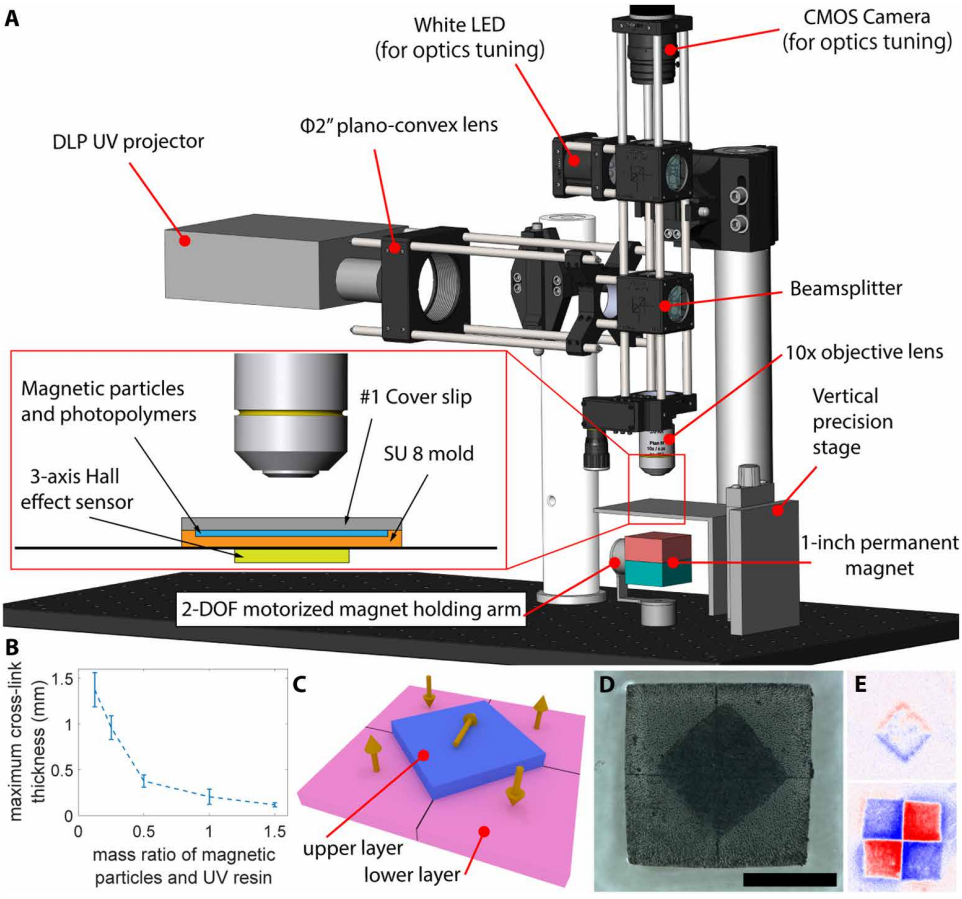

Fig. 1. Schematic representation of the system for patterning discrete 3D magnetization. (**A**) Physical apparatus for patterning permanent magnetic particles in a UV-curable elastomeric matrix composite. DOF, degree of freedom. (**B**) Experimentally measured maximum cross-link thickness with respect to magnetic particle concentration. Error bars indicate SD. (**C**) Schematic representation of a dual-layer structure that has both horizontal and vertical magnetization components. Yellow arrows show the direction of magnetization patterned in each block. (**D**) Top view image of the dual-layer structure fabricated. Scale bar, 2 mm. (**E**) Out-of-plane magnetic flux distribution measured at the near surface of each layer separately using a magneto-optical sensor. The magneto-optical images are taken with the two layers fabricated independently to better visualize the magnetization profile.

Complex magnetic torque-induced deformation

Planar soft materials that have distributed 3D magnetization profiles can bend into predesigned 3D shapes upon the application of a uniform magnetic field and return to the original shape once the field is removed. Figure 2 and fig. S2 show the original states, actuating states, and schematic designs of different types of planar structures. Some of these untethered devices were patterned in a symmetric or centrosymmetric manner so that the net magnetization was aligned with the external magnetic field during actuation, resulting in internal deformation rather than rigid body rotation. As a general design rule, bending requires varying magnetization in the neutral axis plane (Fig. 2, B and C), whereas torsion requires magnetization perpendicular to the neutral axis (Fig. 2E). Structures that contain both parallel and normal magnetization components to the neutral axis yield a combined bending and torsion (Fig. 2F). Furthermore, advanced torque-induced deformation can be achieved by combining these design rules together. Higher-order bending (undulatory bending) is realized by patterning alternating magnetization segments, which generate pairs of counteracting magnetic torques (Fig. 2, A and D). Large-angle (90° to 180°) deflection is realized by the noncontinuum transitions of magnetization angles in the plane of bending (Fig. 2G). By having multiple large-angle deflection structures, planar polymers could fold up to form a spherical hollow space in the center (Fig. 2, H to J). In Fig. 3 (A to D), we provide simulation models to predict the shape changes. In Fig. 3 (E and F), we show that different shape changes for the same tri-arm structure could be achieved by tuning the patterning angles. The capability to pattern arbitrary 3D magnetization and geometries allowed highly deformable millimeter-scale structures under a magnetic field of 20 mT, which is readily available in a general electromagnetic coil system.

Speed-tunable segmented magnetic swimmer

Magnetic microscale swimmers make use of the corkscrew motion (*36*), beating flagellar motion (*37*, *38*), and traveling wave undulatory motion (*29*) for propulsion. Magnetic undulatory swimmers benefit from a simple structure, but the shape of the traveling wave in previous work could not be tuned arbitrarily because of the continuous distribution of magnetization developed by template-aided magnetizing (*29*, *39*). Using the current patterning technique, we present undulatory swimmers that have the same size and volume magnetization but different magnetization pattern, resulting in different shape changes and swimming speeds under a rotating magnetic field. This arbitrary patterning method thus can serve as a versatile fabrication tool for studying underlying physical principles and creating optimized designs with tunable performance.

Figure 4 (A and D) and table S1 show the designs of three types of swimmers fabricated from the same precursor. The swimming speed of each type of swimmer on the water surface was measured under different field strengths and rotating frequencies (Fig. 4C). The theoretical swimming speed of each design is characterized using traveling wave component (TWC) analysis (*39*), a method that evaluates the time-integral propulsive forces and the swimming speed of film-shaped undulatory swimmers. A detailed analysis is provided in text S2 and figs. S3 to S5. In Fig. 4B, the blue dots represent the theoretical deflection amplitude of the swimmers at each phase angle of the applied field, and the size of the equivalent circle serves as an indicator of the amplitude of the traveling wave and thus can serve as a heuristic for propulsive force of the swimmer in one period. The measured swimming speed data show a tendency similar to that of the simulated TWC analysis; type 1 design has an equivalent circle radius of 0.222 mm and thus the fastest swimming

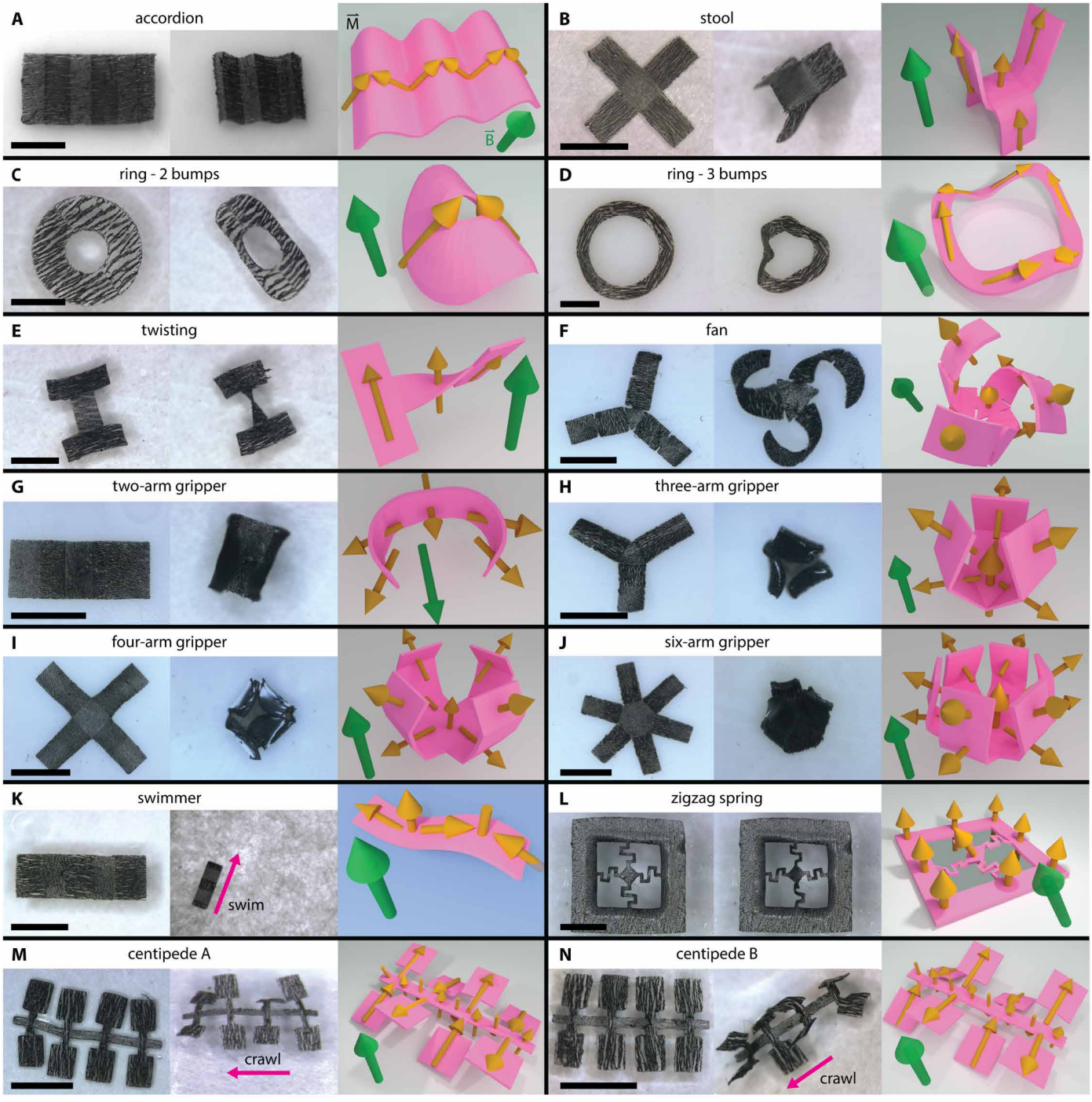

Fig. 2. Flexible magnetic planar structures that have distributed 3D magnetization profiles. Yellow arrows represent the direction of local magnetization, and green arrows represent the direction of the actuating magnetic field. The materials are about 80 μm thick. The actuating magnetic field was 200 mT for "accordion" and less than 20 mT for all the others. All the items presented reversible and rapid transformation between the original shape and the folding shape. Scale bars, 2 mm.

speed, followed by type 2 and type 3 designs. In addition, the fabricated swimmers presented high controllability in an electromagnetic coil system. Figure 4 (E and F) and movie S1 show a swimmer following an M-shaped path using a closed-loop vision feedback. With the surface tension of water surface restricting the movement along the *z* axis, the heading of the swimmer could be controlled by changing the rotating axis of the driving magnetic field. The swimmer was actuated in a 9-mT rotating field at 20 Hz, presenting an average velocity of 3.38 mm/s (78.6% body length) and a maximum deviation of 0.2 mm (4.65% body length).

Multi-arm untethered magnetic microgripper

Grasping capability is among the most useful motions of microrobots, and magnetically actuated grippers have the advantages of being

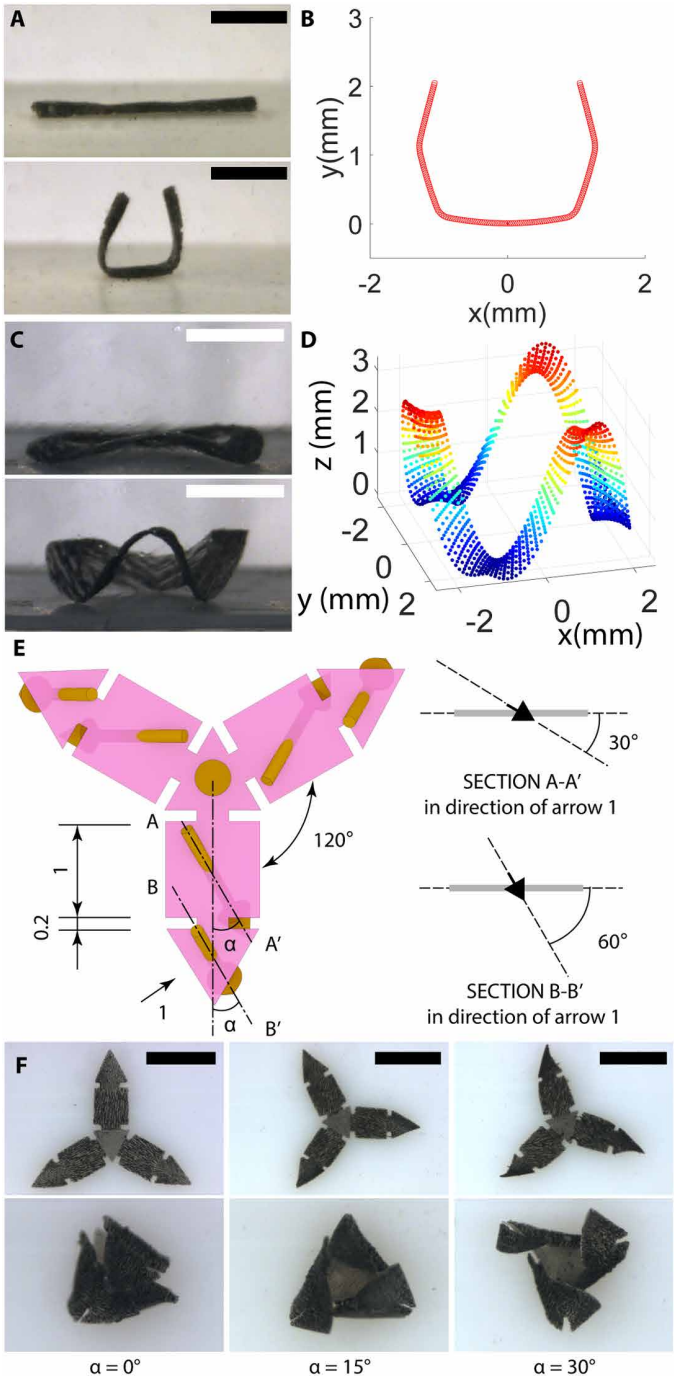

Fig. 3. Models for predicting the shape changes and capabilities to tune the patterning angle in 3D. (**A**) Side view images showing large-angle deflection under 20 mT. Scale bars, 2 mm. (**B**) Numerical model of the large-angle deflection. (**C**) Side view images showing undulatory bending of a ring under 20 mT. Scale bars, 2 mm. (**D**) Simulation of the ring using the finite element method. (**E**) Geometry, dimension, and the magnetization profile of the tri-arm structure. Unit, mm. (**F**) Top view images of the tri-arm structures that bear different magnetization profiles. They were actuated under a 20-mT magnetic field out of the plane. Scale bars, 2 mm.

untethered and responsive. However, existing power grasping magnetic grippers can be fabricated only by manual assembly of magnetic components, which poses a great challenge to scaling and batch fabrication (*33*, *34*). Using the method presented in this work, we achieved one-process fabrication of magnetic microgrippers that have a configurable number of arms to target various cargos shapes (Fig. 5D). The fabrication time was also substantially decreased; it took less than 20 min to fabricate one four-arm magnetic gripper, as opposed to 8 hours using the previous method (*34*) because of the manual assembly process (text S3).

Figure 5A shows the design of a magnetically actuated six-degree-of-freedom microgripper. Here, six actuated degrees of freedom refer to translation in three dimensions, pitch, yaw, and grasping motion. The microgripper consists of a base segment and several arms to enclose the cargo. Once the arms are folded, the gripper can be modeled as a rigid object and can locomote using rolling motion or the magnetic gradient pulling force. In movie S1, we present the teleoperation of a microgripper as a mobile microrobot. Figure 5 (B and C) shows the transportation of a green triangular prism-shaped polydimethylsiloxane cargo onto a 15° slope that simulated the terrain of unstructured environments. The cargo and the gripper began lying prone on the substrate in silicone oil, and then the gripper folded up and rolled toward the cargo under a rotating magnetic field. The gripper picked up the cargo using the pinching force at the tips, turned itself upside down, and secured the cargo using power grasping. Once it reached the target position, we reversed the direction of the magnetic field to release the cargo and rolled the gripper back to the home position.

Multi-legged paddle-crawling robot

For small-scale robots, walking on a 2D surface requires breaking strong surface adhesion using techniques, such as induced vibration (*40*), stick-slip–based motion (*41*), and surface engineering that provides superior adaptivity (*42*). From the perspective of motions, flexible magnetic microrobots typically crawl using inchworm motion, traveling wave motion (*31*), and continuous inverted pendulum motion (*42*). Here, we show the paddle-crawling motion of a multi-legged robot under a rotating magnetic field. The walking gait of the robot was programmed by patterning alternating discrete magnetization in the legs.

Figure 6 (A and B) shows the design and the locomotion mechanism of an eight-legged paddle-crawling robot. Bearing alternating magnetization in the legs, the robot can stand on legs with its body up and move forward using the stroke action under a rotating magnetic field. The stroke action involves the arms moving forward alternately with the legs kicking the ground throughout the stroke. Propulsive forces were generated by a combination of ground friction and fluid drag. Friction-based propulsion was dominant when the robot sank to the bottom of the liquid, whereas drag-based propulsion was dominant when the robot stayed off the ground. Video of the paddle-crawling motion and the velocity of the multi-legged robot are presented in movie S1 and text S4. The robot bore an alternating magnetization along the body to make the net magnetization close to zero, which prevented the robot from somersaulting during lateral movement. The turning motion of the robot is presented in text S5. Using a joystick controller, we could achieve controlled motion of the robot in a small confined microchannel (Fig. 6, D and E, and movie S1).

Remote laser steering micromirror mount

UV curing allows direct printing of submillimeter-scale intricate features and tiny joints on a substrate without a microassembly process.

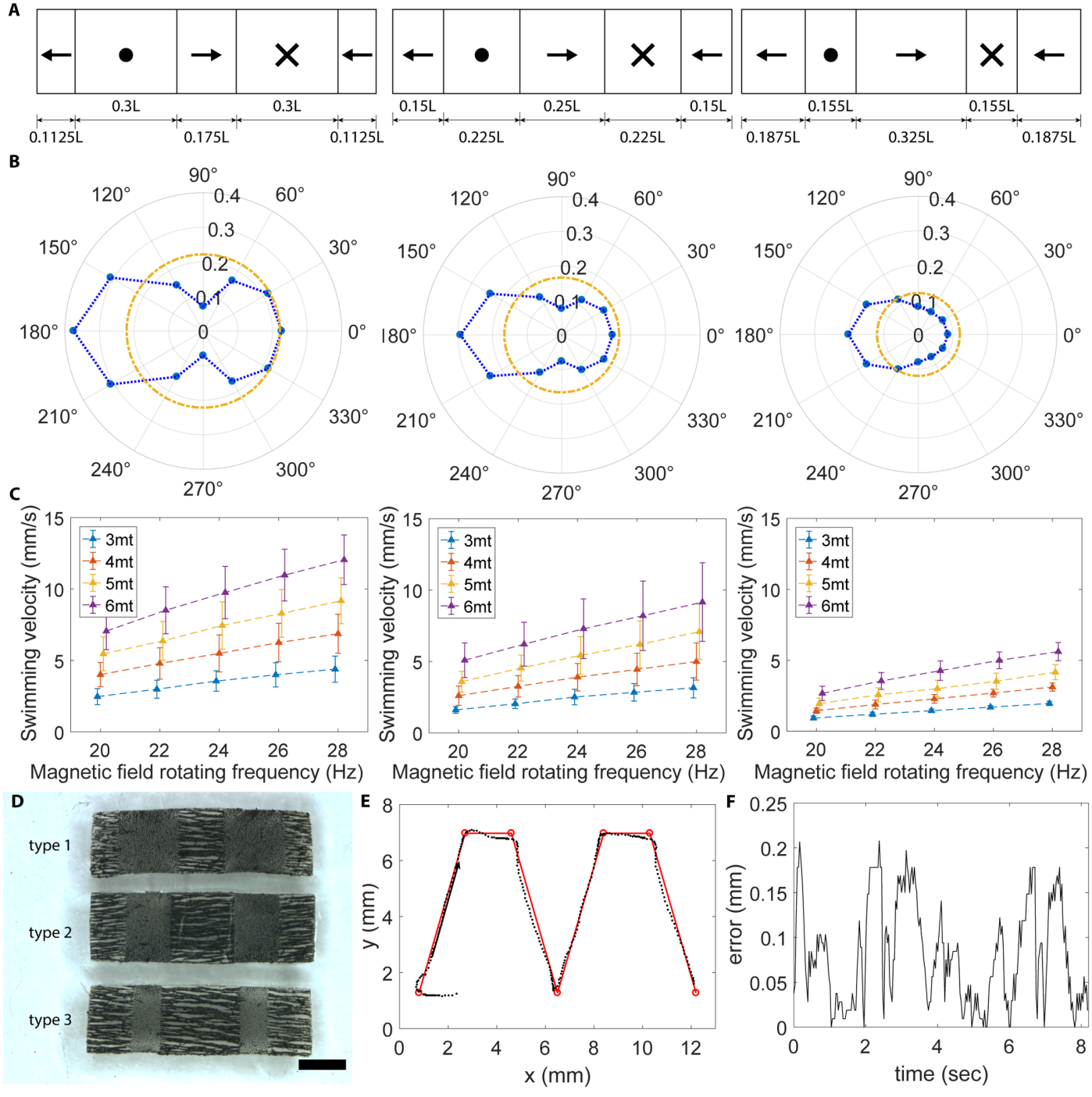

Fig. 4. Millimeter-scale segmented magnetic swimmer. (**A**) Magnetization profiles of three types of swimmers. The body length *L* is 4.5 mm. (**B**) Simulated TWC analysis of the swimmers. Blue markers represent the deformation at each phase, and the yellow dashed lines represent the equivalent deformation circle in one period. (**C**) Experimental swimming speed of the swimmers under different conditions. Solid triangles represent the average of six samples, and error bars represent their SDs. (**D**) Segmented swimmers fabricated from the same precursor in one process. Scale bar, 1 mm. (**E**) Path following of a magnetic swimmer. (**F**) Path following error of a magnetic swimmer, corresponding to the path shown in (E).

With these tiny joints and patterned magnetization, we could fabricate untethered compact devices that have controllable minimal elastic deformations. To demonstrate this capability, we show a two-degree-of-freedom magnetic mirror mount that achieved high precision of motion.

Figure 7A shows the design of an untethered mirror mount. The structure comprised a central stage for the mirror and four spring joints connected to the base. The tilting angle of the mirror could be controlled using a horizontal magnetic field, and it turned to the original position when the field was removed. To demonstrate the

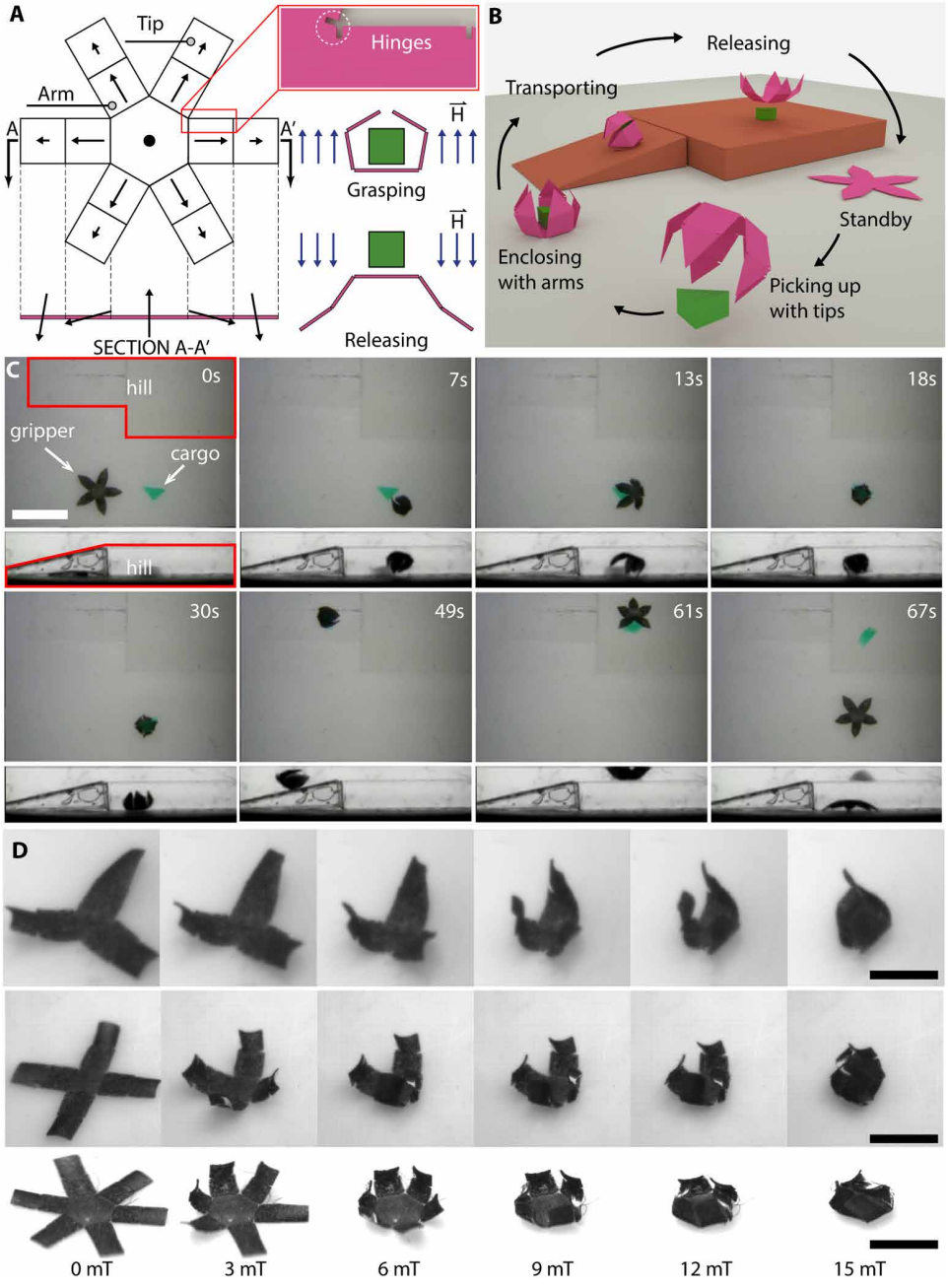

Fig. 5. Untethered multi-arm magnetic microgripper. (**A**) Geometry, magnetization profile, and working mechanism of a magnetic microgripper. Black arrows represent the direction of local magnetization in each part, and blue arrows represent the actuating magnetic field. (**B**) Illustration of the cargo transportation task. (**C**) Top view and side view images of the cargo transportation task in silicone oil (20 cSt; Sigma-Aldrich). Silicone oil is used to lift the body weight and to slow down the shape changes of the gripper to make open-loop control easier. Scale bar, 5 mm. (**D**) Close-up images of different microgrippers at various field strengths. Scale bars, 2 mm.

repeatability and accuracy, we performed an open-loop trajectory after experiment using a laser pointer in a coil system (Fig. 7, B and C). The reflected laser fell on the 20-mm by 20-mm region of a laser viewing card, and the position of the reflected laser was interpreted to the magnetic field using bilinear interpolation in the region of interest. We generated a time-varying magnetic field to draw a T-shaped trajectory and a star-shaped trajectory on the laser viewing card at 0.5 and 0.2 Hz, respectively (Fig. 7D and movie S1). The root mean square (RMS) accuracy (deviation from the desired trajectory) and the RMS precision (deviation from the mean trajectory) are summarized in Table 2. At frequencies higher than 0.5 Hz, the deviation from the desired trajectory became larger because of the momentum of the mirror.

Magnetization verification

The performance of a soft-bodied magnetic actuator depends on the precise patterning of magnetic particles. For example, the microgripper design here required 90° in the base block, −30° in the arm blocks, and −60° in the tip blocks to function properly. We evaluated the patterning accuracy by viewing the distribution of the magnetic flux at sample surfaces using a magneto-optical sensor (MagView S, Matesy GmbH). The measured data were compared with a magnetic dipole array–based model (text S6 and fig. S9), in which we assumed that the magnetic moment density in the material was uniform.

Figure 8 shows the out-of-plane component of the magnetic flux 60 μm away from the sample surface. In Fig. 8 (A to C), the measured magnetic flux density curves show good shape agreement with the model, demonstrating the capability of the proposed method to pattern the magnetization angles precisely. In Fig. 8 (E and F), we magnetically encoded a quick response (QR) code in a 5-mm by 5-mm region on a sheet of polymer. It shows that the precise magnetization feature size of 250 μm could be achieved using this technique, with clearly defined boundaries and sharp edges.

DISCUSSION

In this work, we developed a UV lithography–based method for patterning permanent magnetic particles in planar composite materials, making it possible to fabricate actuators that have programmable 3D magnetization profiles, complex geometries, and thus new types of mechanical motions. This fabrication technique has potential to change the way we design and fabricate flexible microrobots; moreover, we can use it to extend the functionalities of existing miniaturized devices. Although we focus here on patterning magnetization in planar materials, our approach can be extended to 3D media using

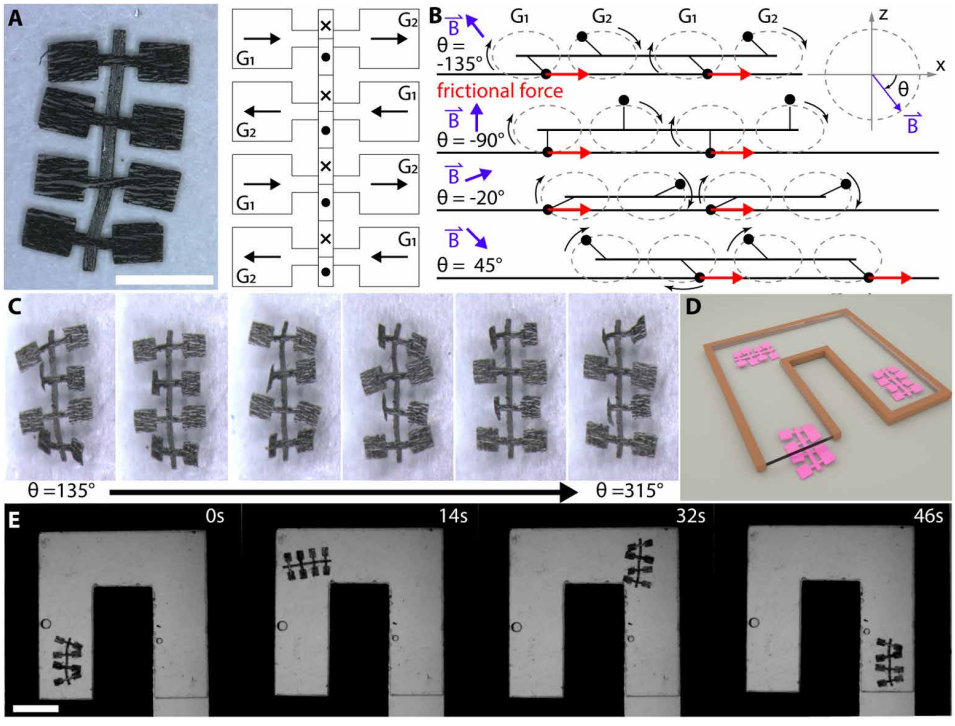

Fig. 6. Multi-legged paddle-crawling robot. (**A**) Image and magnetization profile of a paddle-crawling robot. Local magnetization is denoted by black arrows. When the legs labeled G_1 perform power strokes, the legs labeled G_2 perform recovery strokes, and vice versa. Scale bar, 2 mm. (**B**) Schematic representation of the gait from the side. (**C**) Top view images of the robot at different phases. (**D**) Illustration of the microchannel. The cross section of the channel is 4.7 mm by 1.0 mm. (**E**) Top view images showing the locomotion of the robot in a microchannel filled with silicone oil (20 cSt; Sigma-Aldrich). Silicone oil was used to lift the body weight and to slow down the stroke motions of the robot so that the camera could capture the motion clearly. The stroke motions and the velocity of the robot were faster in water. Scale bar, 4 mm.

Table 2. Trajectory after results. Data were recorded with a 30-frames per s CMOS camera; each has no less than 10 cycles.

Trajectory	Frequency (Hz)	Path length (mm)	RMS accuracy (mm)	RMS precision (mm)
T	0.05	61	1.78 ± 2.46	0.10 ± 0.14
T	0.5	61	1.76 ± 2.42	0.10 ± 0.13
Star	0.05	72	1.72 ± 2.60	0.08 ± 0.11
Star	0.2	72	1.73 ± 2.49	0.62 ± 0.79

layer-by-layer curing, which is commonly used in stereolithography-based 3D printing. Multilayer 3D architectures with programmable 3D magnetization profiles suggest new possibilities for applications in soft robotics and biomedical devices.

Typical stereolithography-based printing can achieve a feature size of several micrometers, but the theoretical feature size in the magnetic patterning method presented in this work is limited by the size of the included permanent magnetic particles (5 μm in this work). The assumption of homogeneous magnetic moment density does not hold if the size of individual magnetization area begins to approach the scale of the particles; in addition, because the particle size imposes a limit to the thickness of the fabricated product, the microrobots cannot be scaled down arbitrarily small, although the assumption is valid. In practice, considering the particle size distribution and irregular particle shapes, we recommend a magnetization feature size roughly one order of magnitude bigger than the particle size to maintain reasonably homogeneous magnetic moment density.

Biocompatibility is also a critical factor for successful application in biomedical use. In this work, the NdFeB permanent magnetic particles were securely encased by cured polymer composites, so that the particles were not in direct contact with the environment to harm biological tissue. In addition, the patterning technique is transferrable to most UV-curing polymers, so different encasement materials may be chosen according to the temperature and acidity of the working environment to ensure safety. To reduce heavy metal toxicity, samarium cobalt or ferrite permanent magnetic particles may be substituted for NdFeB magnetic particles. Typical use of small-scale robots in biological application inside the human body would require removal from the body upon completion of their tasks for safer robot-human interaction.

MATERIALS AND METHODS

Preparation of materials

Permanent magnetic particles that have an average diameter of 5 μm (NdFeB, MQFP-15-7, Magnequench) were premagnetized in a 1.1-T uniform magnetic field between two N52 1-inch permanent magnets with a 3-mm gap. Acquiring saturation remanence, the magnetic particles were mixed sufficiently with UV resin (DLP/stereolithography 3D printer UV resin, flexible type, GC3D-EBE) in a mass ratio of 1:1 to form a homogeneous magnetic slurry. To ensure particle dispersion, we prepared 0.5 g of magnetic slurry on a glass slide and used a glass rod to stir it constantly for 3 min. The magnetic slurry was placed in a vacuum degassing chamber for 1 min to remove the bubbles. Then, the magnetic slurry was loaded into a negative SU8 mold (6 mm by 6 mm by 0.08 mm) prepared using photolithography. The thickness of the SU8 photoresist layer determined the thickness of the final product. The magnetic slurry was covered by a no.1 microscope coverslip (22 mm by 22 mm by 0.15 mm), and the substrate was mounted to the center of the fabrication stage.

Physical apparatus

Figure 1A and fig. S10 show the physical apparatus for patterning magnetic particles in UV resin. The apparatus consisted of a DLP-based lithography system and a magnetic field generator. They were controlled by a computer for automating the fabrication process. A

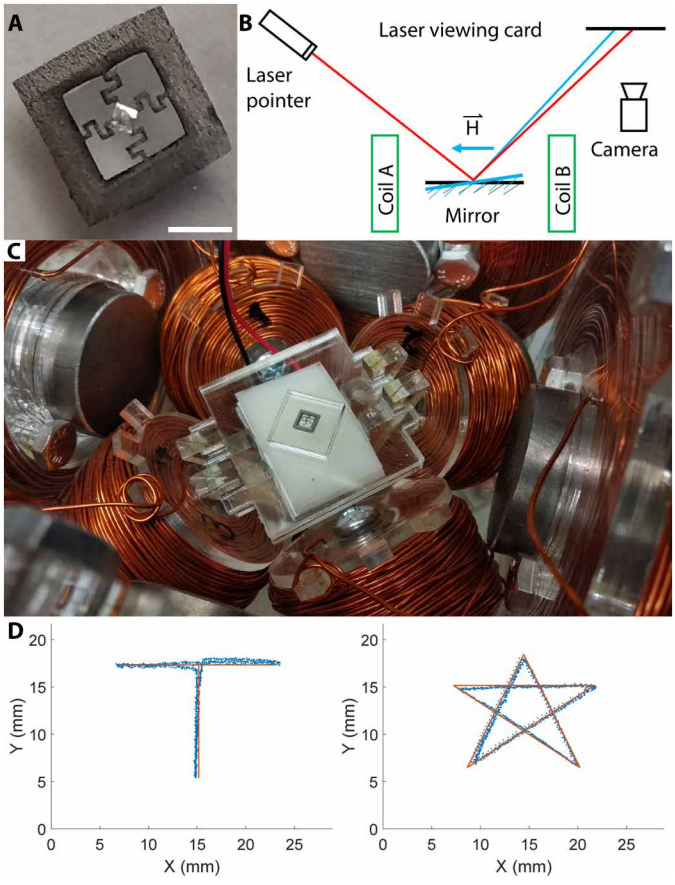

Fig. 7. Untethered magnetic mirror mount for laser steering. (**A**) Close-up image of the mirror mount with a tiny mirror mounted at the center. The magnetization profile of the structure is shown in Fig. 2L. Scale bar, 2 mm. (**B**) Schematic representation of the laser steering experiment. (**C**) Coil system used in the experiment (*43*). (**D**) Target trajectories (orange) and experimental trajectories (blue) of the laser. The T-shaped and star-shaped trajectories are tracked at 0.5 and 0.2 Hz, respectively.

detailed schematic diagram of the hardware connection and signal flow is in text S7 and fig. S11.

The DLP-based lithography system comprised a UV DLP projector (DLP LightCrafter 4500, modified with a 405-nm light engine, Texas Instruments), a plano-convex lens (Ø50.8 mm, f = 75.0 mm; N-BK7, Thorlabs), two cube-mounted nonpolarizing beamsplitters, a Nikon TU Plan Fluor 10×/0.30 microscope objective lens, and a vertical precision stage. A complementary metal-oxide semiconductor (CMOS) camera was installed above the beamsplitter, vertically aligned with the objective lens and the fabrication stage for focus adjustment. With a digital micromirror array in the DLP projector serving as a photomask, the binary image generated by the computer passed through the projector aperture, the plano-convex lens, and the objective lens, forming a demagnified image in the workspace (about 6.0 mm by 6.0 mm) on the object plane. The height of the fabrication stage could be adjusted by the vertical precision knob to bring the object image into focus.

The magnetic field generator comprised an N52 1-inch permanent magnet, two stepper motors, and a three-axis magnetic field sensor (TLV493D-A1B6, Digi-Key). The permanent magnet was held in a way that the center of the magnet was fixed but the azimuthal and polar angles could be independently controlled by two motors. The permanent magnet was placed 4.5 cm under the fabrication stage so that it generated 80- to 160-mT magnetic flux density in the workspace area depending on the magnet orientation. We assumed that the direction and the strength of the magnetic field in this area were nearly uniform. On the basis of the magnetic dipole model and the feedback data from the three-axis magnetic field sensor, we could generate a magnetic field to precisely reorient the premagnetized particles in the slurry and bring them into alignment with any 3D direction.

In its current state, the proposed patterning system has two major problems. First, the size of the permanent magnet limits the size of the workspace because the magnetic field used to reorient the particles is no longer uniform if the size of the workspace is increased. Second, the fabrication stage is not motorized so it can only pattern magnetization in planar materials. In text S1, we introduce a manual material feeding approach for multilayer patterning and discuss how the physical apparatus can be further improved.

Fabrication procedure

The substrate was placed at the center of the fabrication stage, vertically aligned with the objective lens and the magnetic field sensor. Patterning of local magnetization involved two steps: reorientation of included magnetic particles and selective curing of UV resin. First, the stepper motors oriented the permanent magnet to generate the desired magnetic field, which reoriented all the premagnetized magnetic particles in the magnetic slurry. Once the motors reached the desired configuration, both motors performed a damped oscillation that had an initial amplitude of 15° to bring the particles into alignment faster. After allowing 2 min for particle reorientation, UV light shone on selected regions of the magnetic slurry, initiating polymerization and freezing the magnetic particles within that area. For UV curing, we ran the light-emitting diode of the DLP projector (DLP LightCrafter 4500, modified with a 405-nm light engine, Texas Instruments) for 1.5 s at 62.74% pulse-width modulation duty cycle, which corresponds to a current of 2.71 A and 80 lx illuminance according to the datasheet. The two steps were repeated optionally until all the regions were patterned and cured properly. Movie S1 shows the fabrication procedure of the two-arm gripper presented in Fig. 2G.

Optical system characterization

We used a beam profiler (UV-Spiricon, BGP-USB-SP928-OSI, Ophir) to evaluate the geometrical resolution of the UV light on the object plane. We generated squares of various sizes at the object plane and measured the intensity profiles. In the current configuration of optical components, the system has the geometrical feature size as small as 100 μm by 100 mm on the object plane, according to the 10/90 edge steepness metric (text S8 and figs. S12 and S13). The geometrical resolution at the object plane, however, could be increased at the cost of reducing the size of the workspace area by selecting optical components with a higher magnification.

Strength of the magnetic field applied when curing

In the proposed method, local magnetization is patterned by reorienting the premagnetized particles and then curing the resin with UV light. In the physical reorientation process, viscous drag in the UV resin is the principle effect that hinders particle reorientation. Increasing field strength (but not strong enough to magnetize the particles) or present time in the field could both bring more particles into perfect alignment,

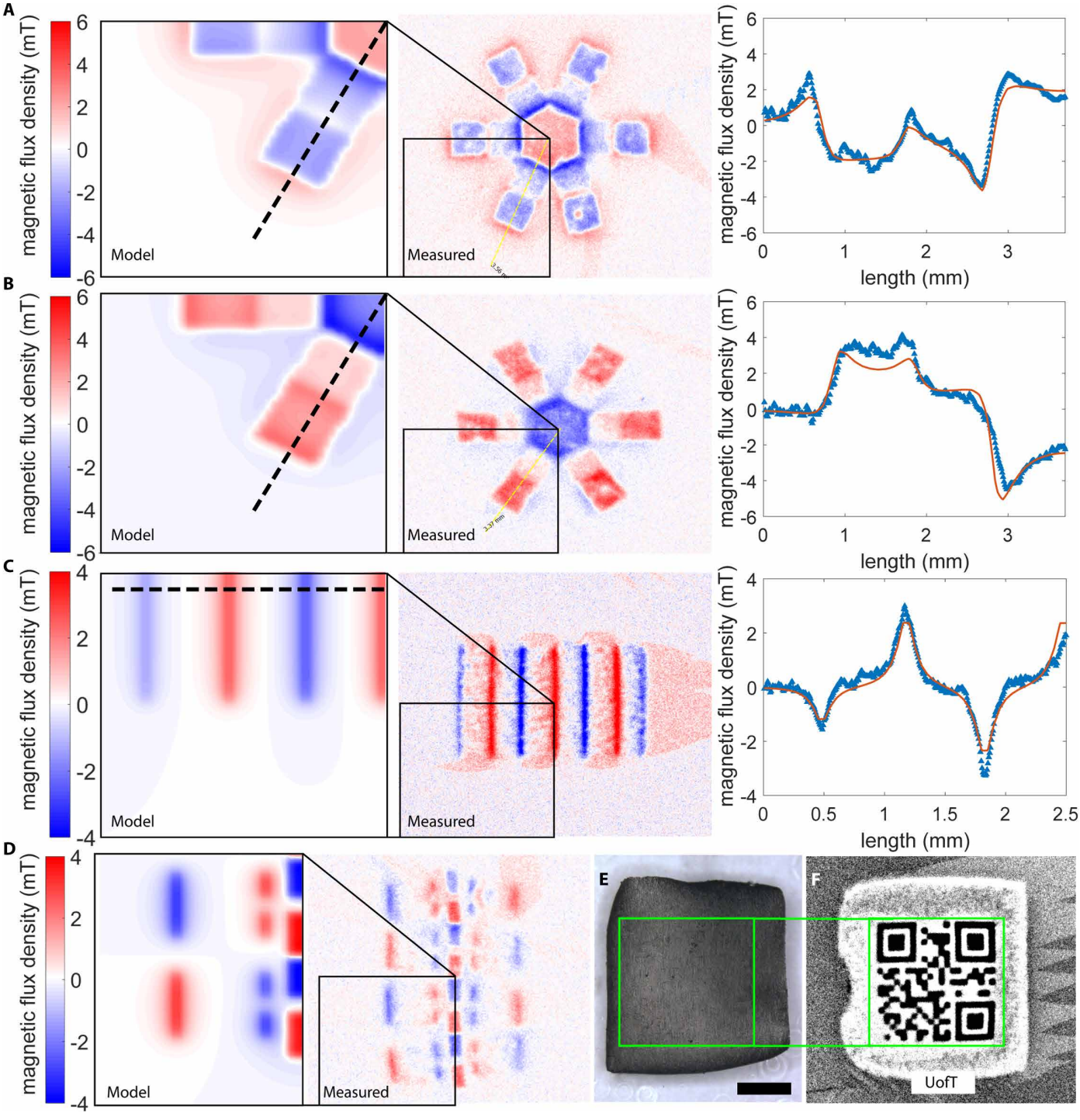

Fig. 8. Distribution of magnetic flux at the near surface of different samples. Modeled magnetic flux distribution, measured magnetic flux distribution, and the fitting results along the black dashed line of (**A**) a six-arm magnetic microgripper (front), (**B**) a six-arm magnetic microgripper (back), (**C**) an accordion, and (**D**) a multi-legged paddle-crawling robot. The data were collected 60 μm away from the sample surfaces. The magnitude of magnetization in the model was fitted to that in the measured data using least squares fitting. (**E**) Thin polymer sheet that carried a magnetically encoded QR code "UofT". Scale bar, 2 mm. (**F**) Magnetic flux measured at the surface of the QR code sample corresponding to (E).

resulting in stronger magnetization after curing. In a preliminary study (text S10), we conducted a controlled experiment to investigate the influence of field strength on resulting magnetization. The results show that field strength of 80 mT and present time for 2 min produced about 75% resulting magnetization compared with that of saturated samples.

Models to predict the shape changes

Finite element analysis was used to predict the shape changes of the materials that have a small deformation. In these models, we used a static structural module in ANSYS with the assumption that the materials have isotropic mechanical property. Young's modulus

E = 331.8 kPa (UV resin was cured using a 405-nm blue light with illuminance of 80 lx and exposure time of 1.5 s; text S9 and fig. S14), Poisson's ratio ν = 0.49, and magnetization M = 24 kA/m (pre-magnetized NdFeB powders and UV resin in a mass ratio of 1:1) were used. For large-angle deflection, we used a custom MATLAB script that conceptually divides the materials into an array of tiny elements, each of which contains a magnetic dipole. The deflection of each element was modeled using Euler-Bernoulli beam theory. The numerical model went through several iterations until the equilibrium state was reached.

Electromagnetic coil system used for actuation

Here, we used a custom Helmholtz electromagnetic coil system for actuating the microrobots, unless noted otherwise. Figure S15 shows the image of the coil system. Each coil was powered by an individual amplifier (30A8, maximum 15-A continuous current, ADVANCED Motion Controls) and controlled by the analog output of a multifunction analog/digital I/O board (Model 826, Sensoray). It could generate a uniform magnetic field up to 20 mT in any direction and up to 50 Hz without a significant drop in field strength. The measured workspace area was about 2.0 cm by 5.5 cm by 4.5 cm.

SUPPLEMENTARY MATERIALS

robotics.sciencemag.org/cgi/content/full/4/29/eaav4494/DC1
Text S1. Manual material feeding for multilayer structures.
Text S2. TWC analysis for magnetic swimmers.
Text S3. Time required for fabricating a four-arm magnetic gripper.
Text S4. Velocity of multi-legged paddle-crawling robot.
Text S5. Turning motion of multi-legged paddle-crawling robot.
Text S6. Magnetic dipole array model for calculating the distribution of magnetic flux.
Text S7. Connection of hardware and flow of control signals.
Text S8. Geometrical resolution of the custom UV lithography system.
Text S9. Measurement of Young's modulus of the material.
Text S10. Magnitude of the magnetization developed by reorienting premagnetized particles.
Fig. S1. Sequence diagram for patterning magnetization in a dual-layer structure.
Fig. S2. Magnetization and dimensions of the devices fabricated.
Fig. S3. TWC analysis of the deformation of type 1 swimmer at different magnetic field angles.
Fig. S4. TWC analysis of the deformation of type 2 swimmer at different magnetic field angles.
Fig. S5. TWC analysis of the deformation of type 3 swimmer at different magnetic field angles.
Fig. S6. Velocity of the multi-legged robot crawling in silicone oil under a 1-Hz rotating magnetic field.
Fig. S7. Velocity of the multi-legged robot swimming (drag-based paddling) at the interface of water and silicone oil under a 2-Hz rotating magnetic field.
Fig. S8. Schematic representation of steering motion of the multi-legged paddle-crawling robot.
Fig. S9. Schematic representation of the magnetic dipole array model.
Fig. S10. Image of the physical apparatus.
Fig. S11. Schematic representation of signal flow and hardware control.
Fig. S12. Intensity profile of squares generated at the object plane.
Fig. S13. Intensity profile of other shapes generated at the object plane.
Fig. S14. Measurement of the stiffness of the material using a microforce sensor.
Fig. S15. Electromagnetic coil system used for actuation.
Fig. S16. Distribution of magnetic flux observed at the near surface of the samples cured in different field strength.
Table S1. Dimension, magnetization, and parameters obtained from TWC analysis.
Table S2. Coefficient of first-order terms of the Fourier series in TWC analysis.
Table S3. Dimensions of the sample used in Young's modulus measurement.
Movie S1 (.mp4 format). Fabrication procedure and demonstration of the microrobots.

REFERENCE AND NOTES

1. B. J. Nelson, I. K. Kaliakatsos, J. J. Abbott, Microrobots for minimally invasive medicine. *Annu. Rev. Biomed. Eng.* **12**, 55–85 (2010).
2. H. Ceylan, J. Giltinan, K. Kozielski, M. Sitti, Mobile microrobots for bioengineering applications. *Lab Chip* **17**, 1705–1724 (2017).
3. D. Cappelleri, D. Efthymiou, A. Goswami, N. Vitoroulis, M. Zavlanos, Towards mobile microrobot swarms for additive micromanufacturing. *Int. J. Adv. Robot. Syst.* **11**, 9 (2014).
4. J. Li, B. Esteban-Fernández de Ávila, W. Gao, L. Zhang, J. Wang, Micro/nanorobots for biomedicine: Delivery, surgery, sensing, and detoxification. *Sci. Robot.* **2**, eaam6431 (2017).
5. H. McClintock, F. Z. Temel, N. Doshi, J.-S. Koh, R. J. Wood, The milliDelta: A high-bandwidth, high-precision, millimeter-scale Delta robot. *Sci. Robot.* **3**, eaar3018 (2018).
6. A. T. Baisch, O. Ozcan, B. Goldberg, D. Ithier, R. J. Wood, High speed locomotion for a quadrupedal microrobot. *Int. J. Rob. Res.* **33**, 1063–1082 (2014).
7. A. Ghosh, C. Yoon, F. Ongaro, S. Scheggi, F. M. Selaru, S. Misra, D. H. Gracias, Stimuli-responsive soft untethered grippers for drug delivery and robotic surgery. *Front. Mech. Eng.* **3**, 7 (2017).
8. J. S. Randhawa, T. G. Leong, N. Bassik, B. R. Benson, M. Jochmans, D. H. Gracias, Pick-and-place using chemically actuated microgrippers. *J. Am. Chem. Soc.* **130**, 17238–17239 (2008).
9. A. Nojoomi, H. Arslan, K. Lee, K. Yum, Bioinspired 3D structures with programmable morphologies and motions. *Nat. Commun.* **9**, 1–11 (2018).
10. J. Li, I. Rozen, J. Wang, Rocket science at the nanoscale. *ACS Nano* **10**, 5619–5634 (2016).
11. F. Soto, A. Martin, S. Ibsen, M. Vaidyanathan, V. Garcia-Gradilla, Y. Levin, A. Escarpa, S. C. Esener, J. Wang, Acoustic microcannons: Toward advanced microballistics. *ACS Nano* **10**, 1522–1528 (2016).
12. D. Ahmed, M. Lu, A. Nourhani, P. E. Lammert, Z. Stratton, H. S. Muddana, V. H. Crespi, T. J. Huang, Selectively manipulable acoustic-powered microswimmers. *Sci. Rep.* **5**, 9744 (2015).
13. M. J. Villangca, D. Palima, A. R. Bañas, J. Glückstad, Light-driven micro-tool equipped with a syringe function. *Light Sci. Appl.* **5**, e16148 (2016).
14. W. Hu, K. S. Ishii, Q. Fan, A. T. Ohta, Hydrogel microrobots actuated by optically generated vapour bubbles. *Lab Chip* **12**, 3821–3826 (2012).
15. X. Yan, Q. Zhou, M. Vincent, Y. Deng, J. Yu, J. Xu, T. Xu, T. Tang, L. Bian, Y.-X. J. Wang, K. Kostarelos, L. Zhang, Multifunctional biohybrid magnetite microrobots for imaging-guided therapy. *Sci. Robot.* **2**, eaaq1155 (2017).
16. C. Peters, M. Hoop, S. Pané, B. J. Nelson, C. Hierold, Degradable magnetic composites for minimally invasive interventions: Device fabrication, targeted drug delivery, and cytotoxicity tests. *Adv. Mater.* **28**, 533–538 (2016).
17. U. Bozuyuk, O. Yasa, I. C. Yasa, H. Ceylan, S. Kizilel, M. Sitti, Light-triggered drug release from 3D-printed magnetic chitosan microswimmers. *ACS Nano* **12**, 9617–9625 (2018).
18. T. Y. Huang, M. S. Sakar, A. Mao, A. J. Petruska, F. Qiu, X. B. Chen, S. Kennedy, D. Mooney, B. J. Nelson, 3D printed microtransporters: Compound micromachines for spatiotemporally controlled delivery of therapeutic agents. *Adv. Mater.* **27**, 6644–6650 (2015).
19. A. Servant, F. Qiu, M. Mazza, K. Kostarelos, B. J. Nelson, Controlled in vivo swimming of a swarm of bacteria-like microrobotic flagella. *Adv. Mater.* **27**, 2981–2988 (2015).
20. X. Yan, Q. Zhou, J. Yu, T. Xu, Y. Deng, T. Tang, Q. Feng, L. Bian, Y. Zhang, A. Ferreira, L. Zhang, Magnetite nanostructured porous hollow helical microswimmers for targeted delivery. *Adv. Funct. Mater.* **25**, 5333–5342 (2015).
21. S. Kim, F. Qiu, S. Kim, A. Ghanbari, C. Moon, L. Zhang, B. J. Nelson, H. Choi, Fabrication and characterization of magnetic microrobots for three-dimensional cell culture and targeted transportation. *Adv. Mater.* **25**, 5863–5868 (2013).
22. M. Medina-Sánchez, L. Schwarz, A. K. Meyer, F. Hebenstreit, O. G. Schmidt, Cellular cargo delivery: Toward assisted fertilization by sperm-carrying micromotors. *Nano Lett.* **16**, 555–561 (2015).
23. I. S. M. Khalil, D. Mahdy, A. El Sharkawy, R. R. Moustafa, A. F. Tabak, M. E. Mitwally, S. Hesham, N. Hamdi, A. Klingner, A. Mohamed, M. Sitti, Mechanical rubbing of blood clots using helical robots under ultrasound guidance. *IEEE Robot. Autom. Lett.* **3**, 1112–1119 (2018).
24. C. Hu, S. Pané, B. J. Nelson, Soft micro- and nanorobotics. *Annu. Rev. Control Rob. Auton. Syst.* **1**, 53–75 (2018).
25. J. Kudr, Y. Haddad, L. Richtera, Z. Heger, M. Cernak, V. Adam, O. Zitka, Magnetic nanoparticles: From design and synthesis to real world applications. *Nanomaterials* **7**, 243–271 (2017).
26. H.-W. Huang, M. S. Sakar, A. J. Petruska, S. Pané, B. J. Nelson, Soft micromachines with programmable motility and morphology. *Nat. Commun.* **7**, 12263 (2016).
27. J. Kim, S. E. Chung, S. E. Choi, H. Lee, J. Kim, S. Kwon, Programming magnetic anisotropy in polymeric microactuators. *Nat. Mater.* **10**, 747–752 (2011).
28. D. Kokkinis, M. Schaffner, A. R. Studart, Multimaterial magnetically assisted 3D printing of composite materials. *Nat. Commun.* **6**, 8643 (2015).
29. E. Diller, J. Zhuang, G. Zhan Lum, M. R. Edwards, M. Sitti, Continuously distributed magnetization profile for millimeter-scale elastomeric undulatory swimming. *Appl. Phys. Lett.* **104**, 174101 (2014).
30. G. Z. Lum, Z. Ye, X. Dong, H. Marvi, O. Erin, W. Hu, M. Sitti, Shape-programmable magnetic soft matter. *Proc. Natl. Acad. Sci. U.S.A.* **113**, E6007–E6015 (2016).
31. W. Hu, G. Z. Lum, M. Mastrangeli, M. Sitti, Small-scale soft-bodied robot with multimodal locomotion. *Nature* **554**, 81–85 (2018).

32. S. Tasoglu, E. Diller, S. Guven, M. Sitti, U. Demirci, Untethered micro-robotic coding of three-dimensional material composition. *Nat. Commun.* **5**, 3124 (2014).
33. E. Diller, M. Sitti, Three-dimensional programmable assembly by untethered magnetic robotic micro-grippers. *Adv. Funct. Mater.* **24**, 4397–4404 (2014).
34. J. Zhang, O. Onaizah, K. Middleton, L. You, E. Diller, Reliable grasping of three-dimensional untethered mobile magnetic microgripper for autonomous pick-and-place. *IEEE Robot. Autom. Lett.* **2**, 835–840 (2017).
35. Y. Kim, H. Yuk, R. Zhao, S. A. Chester, X. Zhao, Printing ferromagnetic domains for untethered fast-transforming soft materials. *Nature* **558**, 274–279 (2018).
36. S. Tottori, L. Zhang, F. Qiu, K. K. Krawczyk, A. Franco-Obregón, B. J. Nelson, Magnetic helical micromachines: Fabrication, controlled swimming, and cargo transport. *Adv. Mater.* **24**, 811–816 (2012).
37. A. M. Maier, C. Weig, P. Oswald, E. Frey, P. Fischer, T. Liedl, Magnetic propulsion of microswimmers with DNA-based flagellar bundles. *Nano Lett.* **16**, 906–910 (2016).
38. I. S. M. Khalil, A. F. Tabak, Y. Hamed, M. E. Mitwally, M. Tawakol, A. Klingner, M. Sitti, Swimming back and forth using planar flagellar propulsion at low reynolds numbers. *Adv. Sci.* **5**, 1700461 (2018).
39. J. Zhang, E. Diller, Untethered miniature soft robots: Modeling and design of a millimeter-scale swimming magnetic sheet. *Soft Robot.* **5**, 761–776 (2018).
40. W. Jing, X. Chen, S. Lyttle, Z. Fu, Y. Shi, D. J. Cappelleri, A magnetic thin film microrobot with two operating modes, paper presented at IEEE International Conference on Robotics and Automation, Shanghai, China, 10 May 2011.
41. C. Pawashe, S. Floyd, M. Sitti, Modeling and experimental characterization of an untethered magnetic micro-robot. *Int. J. Rob. Res.* **28**, 1077–1094 (2009).
42. H. Lu, M. Zhang, Y. Yang, Q. Huang, T. Fukuda, Z. Wang, Y. Shen, A bioinspired multilegged soft millirobot that functions in both dry and wet conditions. *Nat. Commun.* **9**, 3944 (2018).
43. S. Salmanipour, E. Diller, Eight-degrees-of-freedom remote actuation of small magnetic mechanisms, paper presented at IEEE International Conference on Robotics and Automation, Brisbane, Queensland, 21–25 May 2018.
44. R. Dreyfus, J. Baudry, M. L. Roper, M. Fermigier, H. A. Stone, J. Bibette, Microscopic artificial swimmers. *Nature* **437**, 862–865 (2005).
45. T. Qiu, T. C. Lee, A. G. Mark, K. I. Morozov, R. Münster, O. Mierka, S. Turek, A. M. Leshansky, P. Fischer, Swimming by reciprocal motion at low Reynolds number. *Nat. Commun.* **5**, 5119 (2014).
46. Z. Z. Bandic, R. H. Victora, Advances in magnetic data storage technologies. *Proc. IEEE* **96**, 1749–1753 (2008).

Acknowledgments: We thank S. Zhang of Wheeler Microfluidics Laboratory in the University of Toronto for assistance in the optical system design. **Funding:** Support for this project was provided by the Natural Sciences and Engineering Research Council of Canada through the Discovery Grant program grant no. 2014-04703. **Author contributions:** All authors contributed to the conceptualization, methodology, analyses, and writing of the manuscript. T.X., J.Z., M.S., and O.O. performed experiments. E.D. supervised the work. **Competing interests:** T.X., J.Z., and E.D. are inventors on patent application US2018/0354120 submitted by the University of Toronto that covers the design and fabrication of flexible microgrippers. **Data and materials availability:** All data needed to evaluate the conclusions in the paper are present in the paper or the Supplementary Materials. The code used to control the coil system is available under the Massachusetts Institute of Technology (MIT) License at https://github.com/atelier-ritz/CoilSystemPython. The code used to pattern the magnetic particles is available under the MIT License at https://github.com/atelier-ritz/pycrafter4500_stepper-based.

Submitted 23 November 2018
Accepted 18 March 2019
Published 24 April 2019
10.1126/scirobotics.aav4494

Citation: T. Xu, J. Zhang, M. Salehizadeh, O. Onaizah, E. Diller, Millimeter-scale flexible robots with programmable three-dimensional magnetization and motions. *Sci. Robot.* **4**, eaav4494 (2019).

Science Robotics

Millimeter-scale flexible robots with programmable three-dimensional magnetization and motions

Tianqi Xu, Jiachen Zhang, Mohammad Salehizadeh, Onaizah Onaizah, and Eric Diller

Sci. Robot. **4** (29), eaav4494. DOI: 10.1126/scirobotics.aav4494

Science Robotics (ISSN 2470-9476) is published by the American Association for the Advancement of Science. 1200 New York Avenue NW, Washington, DC 20005. The title *Science Robotics* is a registered trademark of AAAS.